



## Article

# Doppler-Spread Space Target Detection Based on Overlapping Group Shrinkage and Order Statistics

Linsheng Bu , Tuo Fu \*, Defeng Chen , Huawei Cao, Shuo Zhang and Jialiang Han

School of Information and Electronics, Beijing Institute of Technology, Beijing 100081, China; lsbu@bit.edu.cn (L.B.); cdf2008@bit.edu.cn (D.C.); 7420200045@bit.edu.cn (H.C.); 7520210067@bit.edu.cn (S.Z.); hjliang@bit.edu.cn (J.H.)

\* Correspondence: futuo@bit.edu.cn

**Abstract:** The Doppler-spread problem is commonly encountered in space target observation scenarios using ground-based radar when prolonged coherent integration techniques are utilized. Even when the translational motion is accurately compensated, the phase resulting from changes in the target observation attitude (TOA) still leads to extension of the target's echo energy across multiple Doppler cells. In particular, as the TOA change undergoes multiple cycles within a coherent processing interval (CPI), the Doppler spectrum spreads into equidistant sparse line spectra, posing a substantial challenge for target detection. Aiming to address such problems, we propose a generalized likelihood ratio test based on overlapping group shrinkage denoising and order statistics (OGSos-GLRT) in this study. First, the Doppler domain signal is denoised according to its equidistant sparse characteristics, allowing for the recovery of Doppler cells where line spectra may be situated. Then, several of the largest Doppler cells are integrated into the GLRT for detection. An analytical expression for the false alarm probability of the proposed detector is also derived. Additionally, a modified OGSos-GLRT method is proposed to make decisions based on an increasing estimated number of line spectra (ENLS), thus increasing the robustness of OGSos-GLRT when the ENLS mismatches the actual value. Finally, Monte Carlo simulations confirm the effectiveness of the proposed detector, even at low signal-to-noise ratios (SNRs).

**Keywords:** Doppler-spread target detection; line spectra; overlapping group shrinkage; order statistics



**Citation:** Bu, L.; Fu, T.; Chen, D.; Cao, H.; Zhang, S.; Han, J. Doppler-Spread Space Target Detection Based on Overlapping Group Shrinkage and Order Statistics. *Remote Sens.* **2024**, *16*, 3413. <https://doi.org/10.3390/rs16183413>

Academic Editor: Carmine Serio

Received: 11 July 2024

Revised: 11 September 2024

Accepted: 11 September 2024

Published: 13 September 2024



**Copyright:** © 2024 by the authors. Licensee MDPI, Basel, Switzerland. This article is an open access article distributed under the terms and conditions of the Creative Commons Attribution (CC BY) license (<https://creativecommons.org/licenses/by/4.0/>).

## 1. Introduction

Space surveillance plays a crucial role in military actions and space combat scenarios, holding a pivotal position in terms of space situational awareness (SSA) [1]. However, the detection of distant or small-sized space targets poses significant challenges for ground-based radar systems due to their weak signals, which often require long-time coherent integration to enhance the signal-to-noise ratio (SNR). Numerous studies based on coherent integration have focused on correcting the range migration (RM) and Doppler frequency migration (DFM) caused by translational motions to accumulate echo energy [2–10]. In reality, space debris has lost attitude and orbit control, exhibiting uncontrolled tumbling behavior [11]. The Delta 4 rocket body (NORAD ID: 40535) was observed exhibiting such tumbling by a long-baseline bistatic radar system using an L-band radio telescope network [12]. Spin, precession, and nutation are typical micro-motions in the midcourse phase of ballistic targets [13], all of which cause the target observation attitude (TOA) to vary relative to the radar line of sight. As the integration time increases, the impact of the TOA resulting from micro-motions or observation geometries on accumulation performance is non-negligible. Although targets may be unresolved in range cells in a narrowband radar system, irregular changes in the TOA could still induce the Doppler spread. On one hand, TOA changes become more prominent with a long coherent processing interval (CPI);

on the other hand, the Doppler resolution improves with increased integration time [14]. Consequently, the target energy may disperse across multiple Doppler cells, necessitating secondary accumulation in the Doppler domain to enhance the detection capability. Assuming that translational motions are precisely compensated, the aforementioned issues arise when detecting Doppler-spread targets, for which theories related to high-resolution range-spread target detection are often adopted.

For spread target detection under the influence of Gaussian noise, if the target scattering characteristics are completely known, an ideal likelihood ratio detector can be constructed, enabling a theoretical analysis of the detection performance. However, the scattering information of targets is usually not fully available in practice, leading to unrealizable test statistics, in which case suboptimal detectors are sought. An energy detector [15], which is independent of prior information, has been used to perform the non-coherent integration of echoes within a certain distance range before detection, demonstrating effective performance in scenarios with evenly distributed energy. But, the energy detector also integrates noise cells that lack target echo signals. This is particularly problematic for targets with sparse energy distribution, where the improvement in signal-to-noise ratio (SNR) is reduced and the detection performance degrades. An M/N detector [16], which operates through binary comparisons, assuming that the number of points exceeding the first threshold within N data points is no less than M, generally exhibited superior detection capabilities in scenarios with sparsely distributed energy. Despite that, the detection performance of an M/N detector heavily depends on the second threshold selection, which will cause significant quantization errors when not appropriately selected. Dai et al. [17] re-arranged the data in the detection window according to their energy, and then integrated the range cells and carried out detection according to their order. This method also suffered from the setting of the detection threshold due to the complexity of the probability distribution of order statistics. In addition, the features of the cross-time–frequency distribution (TFD) of a pair of adjacent received signals were exploited in range-spread target detectors [18,19], which were shown to outperform traditional detectors. Consecutive high-resolution range profiles (HRRPs) have also been utilized for the detection of range-spread targets [20,21]. The detection methods related to the HRRPs leverage the stability of the range profile of wideband radar targets. However, when noise or clutter power is high, the SNR suffers significant loss, which results in the deterioration of detection performance.

In terms of adaptive detection, DeMaio [22] addressed the problem related to the polarimetric adaptive detection of range-spread targets with an unknown covariance matrix. Tang et al. [23] extensively investigated the adaptive detection of range-spread targets with noise covariance sharing block-diagonal structures, and proposed two categories of invariant detectors through adopting the invariance principle. Adaptive Rao and Wald tests were researched in the context of an unknown covariance matrix in [24]. Moreover, an adaptive double-threshold (DT) detection method was proposed in [25] that fully utilizes the features of HRRPs. However, this approach is computationally intensive and experiences performance degradation at low SNRs.

Furthermore, many detection algorithms have been developed for range-spread targets in scenes with various clutter. For a Gaussian clutter scene, a double-threshold constant false alarm rate (DT-CFAR) detector was proposed by exploiting the scatterer density and amplitude in [26]. Assuming that a set of secondary data is available, adaptive Rao and Wald tests were proposed in [27], resulting in a two-step detection strategy; according to this, an adaptive detector was also proposed by exploiting the persymmetry of the unknown covariance matrix in [28]. For a non-Gaussian clutter scene, Gerlach [29] proposed a scatterer density-dependent generalized likelihood ratio test (SDD-GLRT) using prior knowledge of the spatial scatterer density and the clutter covariance matrix. He et al. [30] proposed order statistics GLRT (OS-GLRT), which essentially assumes that the number of scatterers and secondary data is known. SDD-GLRT and OS-GLRT use prior knowledge of the spatial scatterer density, which is unattainable for targets in space surveillance that are always non-cooperative. Therefore, the detection performance will decrease when there is

a mismatch in prior information. To avoid reliance on prior information, Ren et al. [31,32] proposed an adaptive scatterer estimation GLRT (ASCE-GLRT) by modeling the problem of scatterer estimation in terms of a sparse signal representation, and proposed an adaptive Doppler steering matrix estimation GLRT (ADSME-GLRT) using a sparse Bayesian optimization model, both with available secondary data. Both the methods perform well in detecting sparsely distributed signals but fail to fully exploit the structural information of the sparse signals.

In this work, we investigate the Doppler spread target detection of TOA changes over multiple periods within a CPI. Relevant targets include rapidly spinning space debris, precessional warheads, tumbling rocket bodies, and satellites. After compensating for translational motion and coherent integration, the echo energy is sparsely dispersed in equidistant Doppler cells, which poses significant challenges for target detection. To solve this problem, we first adopt a denoising algorithm. The overlapping group shrinkage (OGS) algorithm was initially proposed by Chen and Selesnick [33] to address signal denoising when large-amplitude coefficients form groups. Chen and Selesnick [34] further introduced non-convex regularization terms to make the total cost function convex, enhancing its performance under sparsity and refining the OGS algorithm. Unlike traditional sparse denoising methods, which treat each coefficient independently, OGS considers groups of coefficients. This grouping helps to preserve the relationships between signal components, which is crucial for accurately recovering the underlying signal structure. He et al. [35] integrated a periodicity-induced OGS (POGS) algorithm into the penalty function to mimic the periodicity of sparse groups for fault detection in rotating machinery. Li et al. [36] devised a non-convex penalty function based on an elastic net and the  $L_p$  norm, proposing a sparsity-enhanced POGS method for detecting weak periodic impulses. Moreover, although order-statistic-based detection methods pose challenges related to their computational complexity and sensitivity to parameter selection, they offer robust performance in noisy and cluttered environments with minimal prior information [17,30].

The main contributions of this article are summarized as follows:

- (1) An interval-adaptive OGS-based denoising algorithm is developed for Doppler-spread line spectra with equidistant sparsity, which performs well in restoring the Doppler cells occupied by line spectra at low SNRs;
- (2) A GLRT based on the order statistics of a denoised Doppler sequence is proposed for target detection, and an analytical expression for the false alarm probability with any combination in the index set is derived.

The remaining sections of this paper are organized as follows: Section 2 presents the signal model. In Section 3, the OGS denoising algorithm is introduced, the denoising process of line spectra with equidistant sparse constraints is deduced, and interval-adaptive steps (as well as the case where the TOA undergoes a non-integer cycle) are provided. Section 4 derives the generalized likelihood ratio detector guided by the order-denoised Doppler signals and provides an analytical expression for the false alarm probability. Section 5 comprehensively evaluates the proposed detector's performance through Monte Carlo simulations and comparisons with several typical GLRT-based detectors. Finally, Section 6 summarizes the paper.

## 2. Signal Model

It is assumed that the target observation attitude (TOA) exhibits periodicity over a coherent processing interval (CPI)  $T_I$  with period  $T_\sigma$  satisfying  $T_r \ll T_\sigma \ll T_I$ , where  $T_r$  represents the pulse repetition time (PRT). For such targets, a common scattering characteristic model is the sinusoidal frequency-modulated signal [37]. Then, the temporal variation in the target's complex scattering factor can be decomposed into several harmonic components. To develop a model suitable for more general periodic signals, this paper relaxes the constraints on the specific positions and amplitudes of the harmonics and retains only the constraint of equidistance [38]. Consequently, the discrete form of the complex scattering factor of the space target in the slow-time dimension can be expressed as

$$x_n = \sum_{l=0}^{L-1} A_l \exp\{j[2\pi(l_0 + l)nT_r/T_\sigma + \varphi_l]\}, n = 1, \dots, N, \quad (1)$$

where  $N$  is the number of pulses;  $L$  represents the harmonic number, which also corresponds to the number of line spectra;  $A_l$  and  $\varphi_l$  denote the amplitude and initial phase of the  $l$ -th harmonic, respectively; and  $l_0$  signifies the starting position of the line spectra. Therefore, when the range and Doppler migration caused by translational motion are precisely compensated, the Doppler spectrum of the multi-pulse coherent integration exhibits sparse equidistant line spectra. The spectrum of the complex scattering factor during a CPI is

$$X(f) = \frac{T_I}{T_\sigma} \sum_{l=l_0}^{l_0+L-1} X_\sigma\left(\frac{l}{T_\sigma}\right) \otimes \text{sinc}(T_I f), \quad (2)$$

where  $\otimes$  denotes a convolution operator;  $X_\sigma(f)$  represents the spectrum corresponding to the complex scattering factor of a single TOA period;  $X(f)$  can be viewed as sampling  $X_\sigma(f)$  at intervals of  $1/T_\sigma$  with a resolution of  $1/T_I$ ; and its discrete form manifests as  $L$  equidistant line spectra with an interval of  $I = T_I/T_\sigma$ . For convenience,  $T_I/T_\sigma$  is first assumed to be an integer in this context, while the case where  $T_I/T_\sigma$  is a non-integer is discussed in detail in Section 3.4. Figure 1 depicts the normalized echo signals in the slow-time and Doppler dimensions at an SNR of  $-12$  dB with eight line spectra. In this study, the SNR is defined as the ratio of the total energy of all line spectra to the average noise energy before coherent integration, denoted as

$$\text{SNR} = 10 \log \left( \frac{1}{\sigma^2} \sum_{l=0}^{L-1} A_{dl}^2 \right), \quad (3)$$

where  $\sigma^2$  signifies the average noise energy in the slow-time domain.

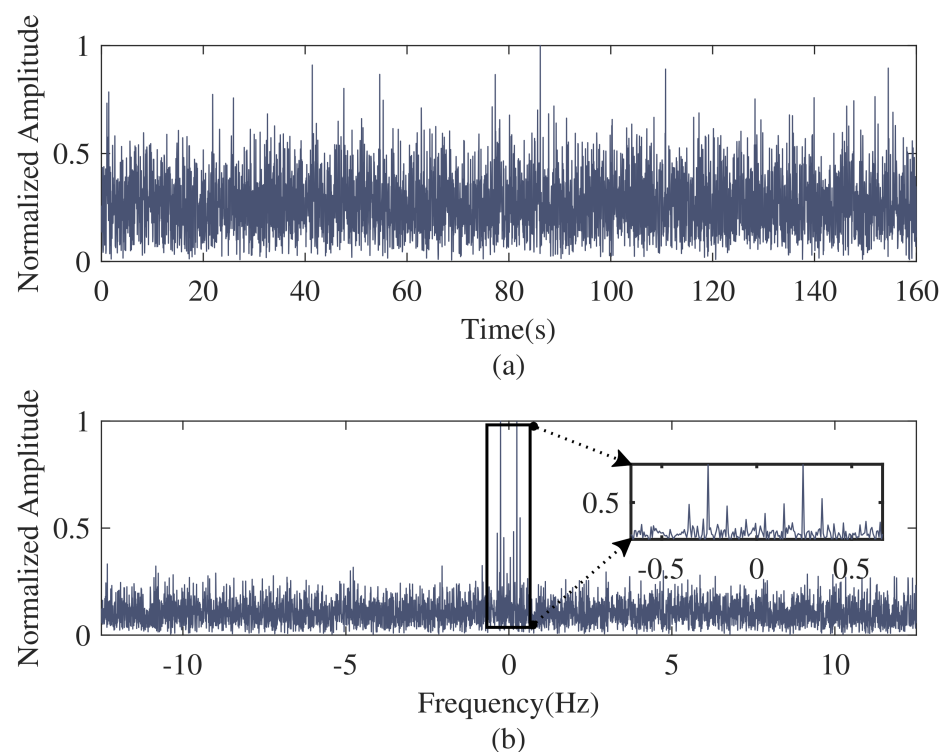


**Figure 1.** Normalized echo signals with  $\text{SNR} = -12$  dB,  $L = 8$ : (a) slow-time domain. (b) Doppler domain.

The following research is carried out in the Doppler domain, in which the Doppler noisy observation vector is represented as

$$\mathbf{Y} = \mathbf{X} + \mathbf{W}, \quad (4)$$

where  $\mathbf{Y} = [y_1, \dots, y_N]^T \in \mathbb{C}^N$  denotes the Doppler noisy observation vector,  $\mathbf{X} = [x_1, \dots, x_N]^T \in \mathbb{C}^N$  represents the equidistant sparse line spectra in the Doppler domain, and  $\mathbf{W} = [w_1, \dots, w_N]^T \in \mathbb{C}^N$  is the complex Gaussian white noise, the variance of which, denoted as  $\sigma_w^2$ , is assumed to be estimated from reference Doppler cells without target echoes.

### 3. Denoising Based on Overlapping Group Shrinkage

In this section, the fundamental theory of the overlapping group shrinkage (OGS) algorithm is briefly introduced. Subsequently, the denoising process for a complex sequence based on OGS constrained by equidistant sparsity and a solution to the convex problem are presented. Then, an adaptive interval adjustment strategy is proposed for the situation where the intervals between the line spectra are unknown. Finally, we discuss the case where the TOA within a CPI presents a non-integer number of cycles.

#### 3.1. Overlapping Group Shrinkage

The OGS algorithm can preserve the correlation between signals, effectively inducing a specific sparse structure in them. Its objective function is typically formulated as a convex function and is solved using the majorize–minimization (MM) iterative algorithm, the core principle of which is successive upper-bound minimization. It involves devising a series of approximate optimization functions to bound the original function from above and then iteratively minimizing this sequence to converge toward the optimal solution of the original objective function. This problem can be described as estimating a sparse signal  $\mathbf{x}$  from a noisy observation vector  $\mathbf{y}$  as follows:

$$\mathbf{x}^* = \arg \min_{\mathbf{x} \in \mathbb{R}^N} \left\{ \mathcal{J}_0(\mathbf{x}) = \frac{1}{2} \|\mathbf{y} - \mathbf{x}\|_2^2 + \lambda \sum_{n=1}^N \phi \left( \left[ \sum_{k=1}^K x_{n+k}^2 \right]^{1/2}; a \right) \right\}, \quad (5)$$

where  $\mathcal{J}_0$  represents the objective function,  $K$  is the size of a group,  $\lambda$  is a regularization parameter, and  $\phi: \mathbb{R} \rightarrow \mathbb{R}_+$  denotes the penalty function, with the parameter  $a$  inducing corresponding sparsity in the optimization problem, which is subject to the conditions listed in Appendix A.

Common penalty functions used to promote sparsity include the logarithmic penalty, arctangent penalty, and first-order rational penalty. When the parameter of the penalty function approaches zero, the aforementioned penalty functions approximate the absolute value function, making the absolute value function a type of penalty function that satisfies the specified conditions. With the same value of  $a$ , the arctangent penalty function exhibits the most concavity, with non-convex regularization being more effective in accurately recovering sparse signals than convex regularization. Therefore, this study proceeds with subsequent research based on the arctangent penalty, as presented in Equation (6). Detailed analyses focused on parameter selection for  $a$  and  $\lambda$  have been presented in [35,39].

$$\phi(x; a) = \frac{2}{\sqrt{3}a} \left( \arctan \left( \frac{1 + 2a|x|}{\sqrt{3}} \right) - \frac{\pi}{6} \right), \quad (6)$$

#### 3.2. Denoising of Line Spectra with Equidistant Sparsity

To induce equidistant sparsity in the Doppler sequence, a  $\{0, 1\}$  binary-weighted sequence is introduced into the OGS model:

$$\mathbf{x}^* = \arg \min_{\mathbf{x} \in \mathbb{R}^N} \left\{ \mathcal{J}_1(\mathbf{x}) = \frac{1}{2} \|\mathbf{y} - \mathbf{x}\|_2^2 + \lambda \sum_{n=1}^N \phi \left( \left[ \sum_{k=1}^K b_k x_{n+k}^2 \right]^{1/2}; a \right) \right\}, \quad (7)$$

$$\mathbf{b} = \underbrace{\left[ \overbrace{1, 0, \dots, 0}^I, \overbrace{1, 0, \dots, 0}^I, \dots, \overbrace{1, 0, \dots, 0}^I \right]}_{K=MI} \quad (8)$$

where  $b_k$ s refer to elements of  $\mathbf{b}$ ,  $\mathbf{b}$  is a binary-weighted sequence, and  $M$  is the number of intervals contained in one group. Following this, for the convenient direct application of the aforementioned reality-based theoretical derivations, the complex Doppler signal is represented as an extended signal stacked with its real and imaginary parts. Equation (4) can then be reformulated as

$$\bar{\mathbf{Y}} = \bar{\mathbf{X}} + \bar{\mathbf{W}}, \quad (9)$$

where

$$\bar{\mathbf{Y}} \triangleq \begin{bmatrix} \text{Re}(\mathbf{Y}^T) & \text{Im}(\mathbf{Y}^T) \end{bmatrix}^T = [\bar{y}_1, \bar{y}_2, \dots, \bar{y}_{2N}]^T \in \mathbb{R}^{2N}; \quad (10)$$

$\bar{\mathbf{X}}$  and  $\bar{\mathbf{W}}$  have the same definitions as above. The extended signal  $\bar{\mathbf{X}}$  is a stack of the real and imaginary parts of the complex domain signal  $\mathbf{X}$ ; as such, the first and second halves of  $\bar{\mathbf{X}}$  possess the same sparse structure. Therefore, we constrain the two parts of the extended signal with the same weighted sequence and substitute Equation (9) into Equation (7), yielding

$$\bar{\mathbf{X}}^* = \arg \min_{\bar{\mathbf{X}} \in \mathbb{R}^{2N}} \left\{ \mathcal{J}(\bar{\mathbf{X}}) = \frac{1}{2} \|\bar{\mathbf{Y}} - \bar{\mathbf{X}}\|_2^2 + \lambda \sum_{n=1}^N \phi \left( \left[ \sum_{k=0}^{K-1} b_k (\bar{x}_{n+k}^2 + \bar{x}_{N+n+k}^2) \right]^{1/2}; a \right) \right\}. \quad (11)$$

$\mathcal{J}$  is strictly convex if  $0 \leq a \leq \frac{1}{\lambda M}$ , which is proven in detail in Appendix B. The detailed derivation for solving problem (11) using the MM method is as follows:

$$\mathbf{u}^{(i+1)} = \arg \min_{\mathbf{u}} \mathcal{H}(\mathbf{u}, \mathbf{u}^{(i)}), \quad (12)$$

where  $i$  denotes the iteration index and  $\mathcal{H} : \mathbb{R}^{2N} \times \mathbb{R}^{2N} \rightarrow \mathbb{R}$  is a majorizer of  $\mathcal{J}$ , which satisfies

$$\begin{aligned} \mathcal{H}(\mathbf{u}, \mathbf{v}) &\geq \mathcal{J}(\mathbf{u}) \\ \mathcal{H}(\mathbf{v}, \mathbf{v}) &= \mathcal{J}(\mathbf{v})' \quad \forall \mathbf{u} \in \mathbb{R}^N. \end{aligned} \quad (13)$$

A majorizer  $\varphi : \mathbb{R} \times \mathbb{R} \rightarrow \mathbb{R}$  of the penalty function  $\phi$  was given in [34]:

$$\varphi(u, v) = \frac{u^2 - v^2}{2v} \phi'(v) + \phi(v), \quad (14)$$

Hence, we define  $\mathcal{H}$  as

$$\mathcal{H}(\bar{\mathbf{X}}, \bar{\mathbf{X}}^{(i)}) = \frac{1}{2} \|\bar{\mathbf{Y}} - \bar{\mathbf{X}}\|_2^2 + \lambda \sum_{n=1}^N \varphi(\xi_n, \zeta_n). \quad (15)$$

In Equation (15),  $\xi_n = \left[ \sum_{k=0}^{K-1} b_k (\bar{x}_{n+k}^2 + \bar{x}_{N+n+k}^2) \right]^{1/2}$  and  $\zeta_n = \left[ \sum_{k=0}^{K-1} b_k (\bar{x}_{n+k}^{(i)2} + \bar{x}_{N+n+k}^{(i)2}) \right]^{1/2}$  represent the  $l_2$  norms of the weighted group for the current and previous iterations, respectively. Therefore, when the binary weight sequence  $\mathbf{b}$  is given,  $\zeta_n$  is only related to the previous iteration value  $\bar{\mathbf{X}}^{(i)}$ . Substituting Equation (14) into Equation (15) and combining the terms unrelated to  $\bar{\mathbf{X}}$  yields

$$\begin{aligned} \mathcal{H}(\bar{\mathbf{X}}, \bar{\mathbf{X}}^{(i)}) &= \frac{1}{2} \|\bar{\mathbf{Y}} - \bar{\mathbf{X}}\|_2^2 + \frac{1}{2} \lambda \sum_{n=1}^N \frac{\xi_n^2 - \zeta_n^2}{\zeta_n} \phi'(\zeta_n) + \phi(\zeta_n) \\ &= \frac{1}{2} \|\bar{\mathbf{Y}} - \bar{\mathbf{X}}\|_2^2 + \frac{1}{2} \lambda \sum_{n=1}^N \frac{\phi'(\zeta_n)}{\zeta_n} \xi_n^2 + \mathcal{C}(\bar{\mathbf{X}}^{(i)}) \end{aligned} \quad (16)$$



Here,  $\mathcal{C}(\bar{\mathbf{X}}^{(i)})$  represents a constant that is not dependent on  $\bar{\mathbf{X}}$ . Further transformations applied to Equation (16) yield

$$\mathcal{H}(\bar{\mathbf{X}}, \bar{\mathbf{X}}^{(i)}) = \frac{1}{2} \|\bar{\mathbf{Y}} - \bar{\mathbf{X}}\|_2^2 + \frac{1}{2} \lambda \sum_{n=1}^N (\bar{x}_n^2 + \bar{x}_{N+n}^2) r_n(\bar{\mathbf{X}}^{(i)}) + \mathcal{C}(\bar{\mathbf{X}}^{(i)}), \quad (17)$$

where

$$r_n(\bar{\mathbf{X}}^{(i)}) = \sum_{j=0}^{K-1} b_j \frac{\phi'(\zeta_{n-j})}{\zeta_{n-j}}. \quad (18)$$

Expanding  $\bar{\mathbf{Y}}$  and  $\bar{\mathbf{X}}$  separately and combining the terms unrelated to  $\bar{\mathbf{X}}$ , Equation (17) is rewritten as

$$\mathcal{H}(\bar{\mathbf{X}}, \bar{\mathbf{X}}^{(i)}) = \sum_{n=1}^N \left[ \frac{1 + \lambda r_n(\bar{\mathbf{X}}^{(i)})}{2} (\bar{x}_n^2 + \bar{x}_{N+n}^2) - \bar{y}_n \bar{x}_n - \bar{y}_{N+n} \bar{x}_{N+n} \right] + \mathcal{C}(\bar{\mathbf{X}}^{(i)}, \bar{\mathbf{Y}}). \quad (19)$$

Similarly,  $\mathcal{C}(\bar{\mathbf{X}}^{(i)}, \bar{\mathbf{Y}})$  is a constant only depending on  $\bar{\mathbf{X}}^{(i)}$  and  $\bar{\mathbf{Y}}$ . Equation (19) provides an explicit minimizer. Finally, the MM iteration with respect to Equation (12) is given by

$$\bar{x}_n^{(i+1)} = \begin{cases} \frac{\bar{y}_n}{1 + \lambda r_n(\bar{\mathbf{X}}^{(i)})}, & 1 \leq n \leq N \\ \frac{\bar{y}_n}{1 + \lambda r_{n-N}(\bar{\mathbf{X}}^{(i)})}, & N+1 \leq n \leq 2N \end{cases}. \quad (20)$$

### 3.3. Interval-Adaptive Steps

In practice, the interval between line spectra is generally unknown. Therefore, we propose a traversal estimation method based on maximizing the sum of the largest  $l_2$  norms of weighted groups, allowing us to update the interval in each optimization iteration. Specifically, the  $l_2$  norms of the weighted groups are first sorted in ascending order:

$$\zeta_{(1)} \leq \cdots \leq \zeta_{(n)} \leq \cdots \leq \zeta_{(N)}, \quad (21)$$

Then, the actual interval is subject to maximization of the sum of the  $h$  largest terms of  $\zeta_{(n)}$ ; that is,

$$I^* = \arg \max_{I \in [I_{\min}, I_{\max}], I \in \mathbb{N}} \left\{ \sum_{n=N-h+1}^N \zeta_{(n)} \right\}, \quad (22)$$

where  $[I_{\min}, I_{\max}]$  is the prior information regarding the intervals between line spectra.

The complete interval-adaptive denoising algorithm based on OGS for line spectra with equidistant sparsity is summarized in Algorithm 1. Here,  $\mathbf{X}^*$  denotes the denoised signal, which exhibits an equidistant sparsity in the Doppler domain. Moreover, Figure 2 illustrates a Doppler sequence with  $\text{SNR} = -20$  dB,  $L = 8$ , and  $I = 16$  before and after denoising. The local zoom in Figure 2a reveals that only two main line spectra are visible before denoising, while Figure 2b shows the accurate recovery of all Doppler cells occupied by the line spectra, thus demonstrating the ability of the denoising algorithm at low SNRs. Therefore, from Figure 2c, it is easy to conclude that the interval-adaptive denoising algorithm rapidly converges to the actual interval.

**Algorithm 1** OGS-based interval-adaptive denoising algorithm

---

Input: The noisy observation vector  $\mathbf{Y}$ ; regularization parameter  $\lambda$ ;  
the penalty function  $\phi$ ; prior information of the interval  $[I_{\min}, I_{\max}]$ ;  
Pre-processing with Equation (10);  
Initialization:  $\bar{\mathbf{X}}^{(0)} = \bar{\mathbf{Y}}$ ;  
Procedure:  
**For** each  $i \in [0, iter]$  **do**  
    **For** each  $I = [I_{\min}, I_{\max}]$ ,  $I \in \mathbb{N}$  **do**  
        Compute  $\mathbf{b}$  with Equation (8);  
         $\zeta_n = \left[ \sum_{k=0}^{K-1} b_k \left( \bar{x}_{n+k}^{(i)2} + \bar{x}_{N+n+k}^{(i)2} \right) \right]^{1/2}$ ;  
        Sort  $\zeta_n$  in the ascending order;  
        Estimate interval utilizing Equation (22);  
    **End for**  
    Update weight sequence with Estimated interval;  
    Compute  $r_n(\bar{\mathbf{X}}^{(i)})$  with Equation (18);  
    Iterate  $\bar{x}_n^{(i+1)}$  using Equation (20);  
**End for**  
Output:  $\mathbf{X}^* = \bar{\mathbf{X}}^*(1 : N) + j\bar{\mathbf{X}}^*(N + 1 : 2N)$ .

---

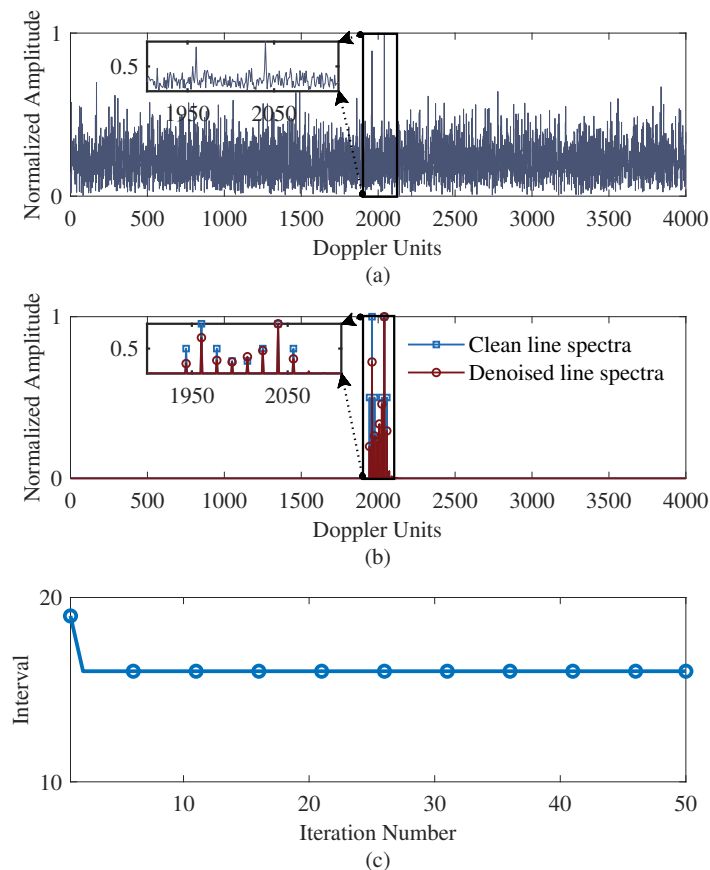


**Figure 2.** Doppler sequence with  $\text{SNR} = -12$  dB,  $L = 8$ ,  $I = 16$ : (a) before denoising. (b) After denoising. (c) Interval-updating process.

### 3.4. Non-Integer Period Case

It is often not feasible to guarantee that a CPI contains integer cycles of TOA variations. In this subsection, the case of non-integer cycles of TOA variations within a CPI is considered.



Let  $I' = T_l/T_\sigma$ , where  $I'$  is a non-integer value. In this case, the line spectra are no longer completely equidistantly sparse in the Doppler domain, with the interval between the  $l$ -th and  $l + 1$ -th line spectra being

$$I(l) = \text{round}(lI') - \text{round}[(l-1)I'], l = 1, \dots, L-1 \quad (23)$$

that is,  $I(l) \in \{\lfloor I' \rfloor, \lceil I' \rceil\}$ . Here,  $\text{round}(x)$  denotes the integer closest to  $x$ ;  $\lfloor x \rfloor$  and  $\lceil x \rceil$  represent the integer flooring and ceiling of  $x$ , respectively.

Nevertheless, the interval between the line spectra oscillates between the two values, resembling a pseudo-equidistant sparsity. According to Section 3.2, the binary weight sequence—which utilizes a unit-step sliding window to capture the sparse structure of the global line spectra—does not necessarily provide a perfect match with the line spectra. To enhance the sparsity of the line spectra, we increase the count of element 1 in the binary weight sequence as follows:

$$\mathbf{b} = \underbrace{\left[ \overbrace{1, 1, 0, \dots, 0}^I, \overbrace{1, 1, 0, \dots, 0}^I, \dots, \overbrace{1, 1, 0, \dots, 0}^I \right]}_{K=MI}, \quad (24)$$

thereby enabling better adaptation to subtle variations in the interval between the line spectra during the sliding window process. Figure 3 illustrates a Doppler sequence with  $\text{SNR} = -20$  dB,  $L = 8$ , and  $I = 17, 17, 16, 17, 16, 16, 16$  before and after denoising. The graph shows that the OGS denoising algorithm can also effectively reconstruct the Doppler cells of the line spectra when the interval oscillates between the two adjacent integers at low SNRs.

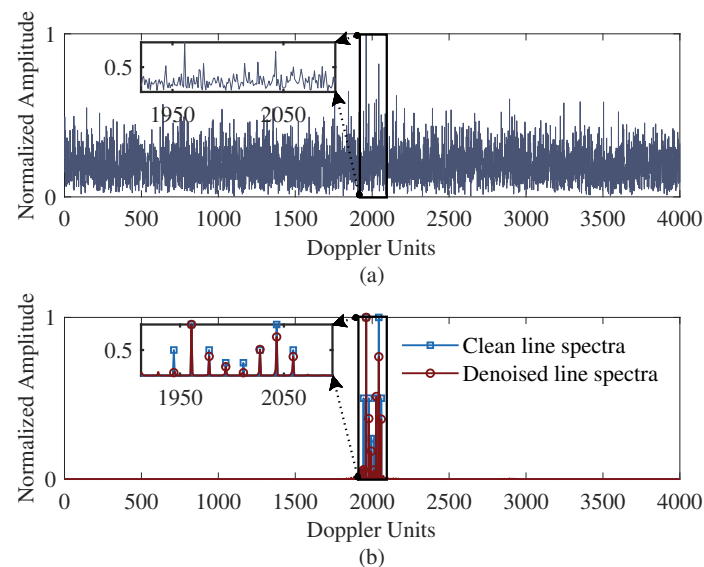


**Figure 3.** Doppler sequence with  $\text{SNR} = -12$  dB,  $L = 8$ ,  $I = 17, 17, 16, 17, 16, 16, 16$ : (a) before denoising. (b) After denoising.

#### 4. OGSos-GLRT Detector

In this section, a generalized likelihood ratio test detector based on overlapping group shrinkage denoising and order statistics (OGSos-GLRT) is presented, as well as its schematic. Furthermore, the probability of a false alarm for a given index set of Doppler cells integrated in the detector is derived.

#### 4.1. The Proposed Detector

The problem of detecting line spectra with equidistant sparsity in the Doppler domain can be formulated as a binary hypothesis:

$$\begin{aligned} H_0 : y_n &= w_n \\ H_1 : y_n &= x_n + w_n, n = 1, \dots, N, \end{aligned} \quad (25)$$

The joint probability density functions (pdfs) under  $H_0/H_1$  are, respectively, denoted as

$$\mathcal{P}_{\mathbf{Y}|H_0}(\mathbf{Y}|H_0) = \frac{1}{\pi^N \sigma_w^{2N}} \exp\left(-\frac{\mathbf{Y}^H \mathbf{Y}}{\sigma_w^2}\right), \quad (26)$$

$$\mathcal{P}_{\mathbf{Y}|H_1}(\mathbf{Y}|\mathbf{X}, H_1) = \frac{1}{\pi^N \sigma_w^{2N}} \exp\left(-\frac{(\mathbf{Y} - \mathbf{X})^H (\mathbf{Y} - \mathbf{X})}{\sigma_w^2}\right), \quad (27)$$

where the superscript  $H$  represents the complex conjugated transpose.

In order to avoid collapsing loss—which refers to processing in which additional noise samples are applied to the integrator—specific Doppler cells are integrated in the likelihood ratio detector. Based on the OGS denoising algorithm introduced in the previous section, the Doppler sequence is denoised to a series of line spectra, and the Doppler cells occupied by the most likely target harmonics are restored. Then, the initial Doppler cells corresponding to some of the largest denoised Doppler observations are selected for the likelihood ratio detector. The generalized likelihood ratio can be expressed as

$$\begin{aligned} \Lambda_{\text{OGSos-GLRT}} &= \frac{\mathcal{P}_{\mathbf{Y}|H_1}(\mathbf{Y}|\hat{\mathbf{X}}, H_1)}{\mathcal{P}_{\mathbf{Y}|H_0}(\mathbf{Y}|H_0)} \\ &= \frac{\prod_{n \in \mathcal{G}} \frac{1}{\pi \sigma_w^2} \exp\left(-\frac{|y_n|^2}{\sigma_w^2}\right)}{\prod_{n \in \mathcal{G}} \frac{1}{\pi \sigma_w^2} \exp\left(-\frac{|y_n - x_n|^2}{\sigma_w^2}\right)} = \sum_{n \in \mathcal{G}} |y_n|^2 \underset{H_0}{\overset{H_1}{\gtrless}} \gamma', \end{aligned} \quad (28)$$

where  $\gamma'$  is the detection threshold and  $\mathcal{G}$  is the index set of Doppler cells integrated in the detector.

#### 4.2. False Alarm Probability

This subsection outlines the process of deducing the formula that correlates the false alarm probability with the detection threshold for OGSos-GLRT. The denoising algorithm discussed above diversifies the cases of the composition of set  $\mathcal{G}$  in the Doppler cells. Here, the false alarm probability for any  $\mathcal{G}$  set can be derived based on the order statistics. Initially,

let  $z_n = \left| \frac{y_n}{\sigma_w / \sqrt{2}} \right|^2, n = 1, \dots, N$ , where  $z_n$  denotes the energy of the Doppler sequence. Then,  $z_n$  follows an exponential distribution with a pdf:

$$\mathcal{P}_z(z) = \frac{1}{2} \exp\left(-\frac{z}{2}\right). \quad (29)$$

The energy order statistics of the noisy observations can be described by ordering  $z_n$ s as

$$0 \leq z_{(1)} \leq \dots \leq z_{(n)} \leq \dots \leq z_{(N)}, \quad (30)$$

and the  $z_{(n)}$  no longer adheres to independent and identically distributed (IID) assumptions. However,  $\delta z_n = (N - n + 1)(z_{(n+1)} - z_{(n)})$  conforms to IID, having a pdf consistent with that of  $z_n$  [40]. Let  $v_n = \delta z_n / c_n, n = 1, \dots, N$  and  $c_n = N - n + 1 / N_{(n, \mathcal{S})}$ , where  $\mathcal{S}$  denotes the indices of  $\{z_n : n \in \mathcal{G}\}$  in  $z_{(n)}$  and  $N_{(n, \mathcal{S})}$  represents the count of elements in

$\mathcal{S}$  that are greater than or equal to  $n$ ; that is,  $\{z_n : n \in \mathcal{G}\}$  in  $z_{(n)}$  and  $\{z_n : n \in \mathcal{S}\}$  in  $z_{(n)}$  belong to the same set of variables and correspond in a one-to-one manner. Then, we have

$\sum_{n \in \mathcal{S}} z_{(n)} = \sum_{n=1}^N v_n$ , and the test statistics of OGSos-GLRT can be rewritten as

$$\Lambda_{\text{OGSos-GLRT}} = \sum_{n=1}^N v_n \underset{H_0}{\overset{H_1}{\geq}} \gamma, \quad (31)$$

where  $\gamma$  is the new detection threshold. As previously stated,  $v_n$ s are independent but not identically distributed, with their pdfs and moment generation functions (MGFs) being pairs of Laplace transforms, respectively, denoted as [30]

$$\mathcal{P}_{v_n}(v_n|H_0) = \frac{c_n}{2} \exp\left(-\frac{c_n v_n}{2}\right), \quad (32)$$

$$\mathcal{M}_{v_n}(s) = E[\exp(-v_n s)] = \frac{c_n}{2s + c_n}. \quad (33)$$

Hence, the MGF of the test statistics of OGSos-GLRT can be denoted as the product of  $\mathcal{M}_{v_n}(s)$ ; that is,

$$\mathcal{M}_{\Lambda_{\text{OGSos-GLRT}}}(s) = \prod_{n=1}^N \mathcal{M}_{v_n}(s) = \prod_{n=1}^N \frac{c_n}{2s + c_n}. \quad (34)$$

Furthermore, the pdf of  $\Lambda_{\text{OGSos-GLRT}}$  under  $H_0$  is the inverse Laplacian transformation of its MGF, which can be expressed as

$$\begin{aligned} \mathcal{P}_{\Lambda_{\text{OGSos-GLRT}}}(\tau|H_0) &= \mathcal{L}^{-1}\left\{\prod_{n=1}^N \frac{c_n/2}{s + c_n/2}\right\} \\ &= \mathcal{L}^{-1}\left\{\sum_{i=1}^k \sum_{j=1}^{m_i} \frac{a_{i,j}}{(s + c_i/2)^j}\right\}, \quad (35) \\ &= \sum_{i=1}^k \sum_{j=1}^{m_i} \left[ \frac{a_{i,j} \tau^{j-1}}{(j-1)!} \exp\left(-\frac{c_i \tau}{2}\right) \right] \end{aligned}$$

where  $\mathcal{L}^{-1}$  denotes the inverse Laplacian operator;  $1 \leq k \leq N$  is the number of poles;  $m_i$  represents the multiplicity of  $c_i/2$ , satisfying  $1 \leq m_i \leq N$  and  $m_1 + \dots + m_k = N$ .  $a_{i,j}$  denotes the coefficients of the rational fraction decomposition, which are expressed as follows:

$$a_{i,j} = \prod_{n=1}^N \frac{c_n}{2} \cdot \frac{1}{(m_i - j)!} \cdot \frac{d^{m_i-j}}{ds^{m_i-j}} \left[ \prod_{i=1}^k \left( \frac{1}{s + c_i/2} \right)^{m_i} \cdot (s + c_i/2)^{m_i} \right] \Big|_{s=-c_i/2}. \quad (36)$$

Overall, the false alarm probability of OGSos-GLRT with the detection threshold of  $\gamma$  is given by Equation (37):

$$\begin{aligned} P_{fa} &= P\{\Lambda_{\text{OGSos-GLRT}} \geq \gamma | H_0\} \\ &= \int_{\gamma}^{\infty} \sum_{i=1}^k \sum_{j=1}^{m_i} \left[ \frac{a_{i,j} \tau^{j-1}}{(j-1)!} \exp\left(-\frac{c_i \tau}{2}\right) \right] d\tau \\ &= \sum_{i=1}^k \sum_{j=1}^{m_i} \sum_{r=0}^{j-1} \exp\left(-\frac{c_i}{2} \gamma\right) \left(\frac{2}{c_i}\right)^{r+1} \frac{a_{i,j} \gamma^{j-1-r}}{(j-1-r)!} \end{aligned} \quad (37)$$

Finally, a schematic of the proposed detection algorithm is shown in Figure 4. Figure 5a illustrates the probabilities of a false alarm versus the detection threshold for random  $\mathcal{G}$ , obtained through both the analytical expression and Monte Carlo simulations. The

result confirms the validity of Equation (37). In addition, the CFAR characteristic of the detection method is also examined by Monte Carlo simulations under different noise power conditions. Figure 5b illustrates the curves of the false alarm probability versus the noise standard deviation with a preset normalized detection threshold, and demonstrates the CFAR characteristic of the algorithm.

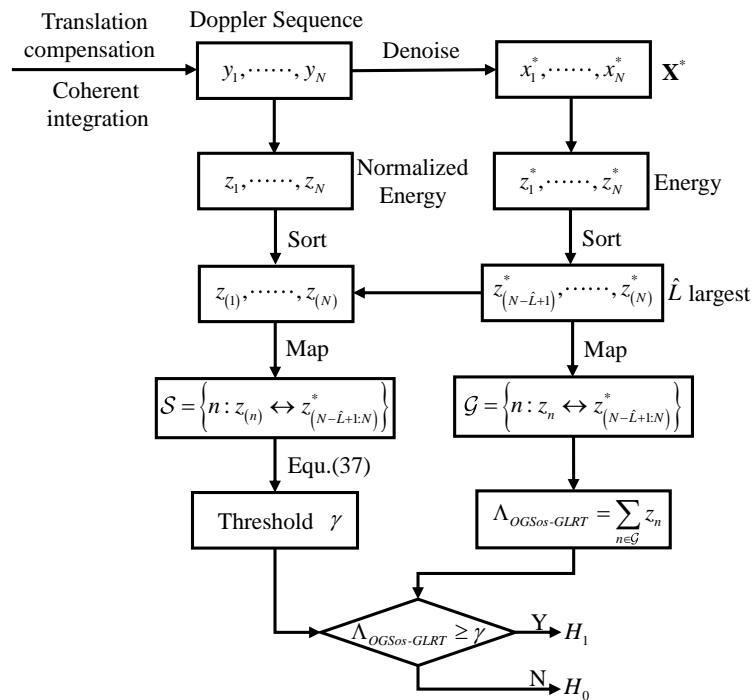


Figure 4. Schematic of the proposed detector.

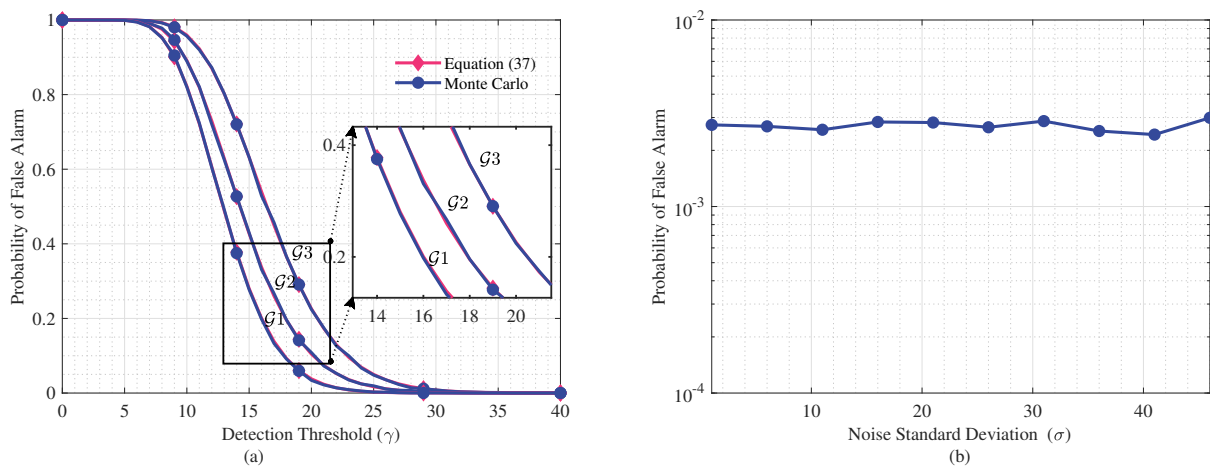


Figure 5. Probability of false alarm: (a) comparison between the analytical expression and Monte Carlo simulations. (b) Sensitivity analysis with respect to noise power.

## 5. Simulations

In this section, Monte Carlo simulations are carried out for MF-GLRT, OS-GLRT, and NLSD-GLRT in addition to OGSos-GLRT in order to comparatively evaluate the performance of the proposed detector. MF-GLRT represents a GLRT, with the actual Doppler cells occupied by the line spectra integrated in the test statistics; it is an ideal likelihood ratio detector, which is generally difficult to achieve in practice. Furthermore, OS-GLRT represents the energy order statistics GLRT [30], while NLSD-GLRT represents a

GLRT that is not dependent on the line spectra characteristics [29]. The test statistics for the three mentioned detectors are defined as

$$\Lambda_{MF-GLRT} = \sum_{n \in \mathcal{K}} z_n, \quad (38)$$

$$\Lambda_{OS-GLRT} = \sum_{n=N-\hat{L}+1}^N z_{(n)}, \quad (39)$$

$$\Lambda_{NLS-GLRT} = \sum_{n=1}^N z_n. \quad (40)$$

where  $\mathcal{K}$  is the index set of Doppler cells occupied by the line spectra.

### 5.1. Simulation Parameters

Except for cases in which specific parameters are investigated for their impact on detection performance and explicitly stated, the simulation parameters were set as shown in Table 1. In the table, the number of pulses,  $T_r$ , and  $T_o$  were all set based on parameters commonly used in real-world space target surveillance scenes. As Equation (2), these parameters determine the interval of the line spectra, which is the ratio of the CPI to the TOA period. The number of line spectra is determined by the electrical size of the space target (the ratio of the target size to the signal wavelength), of which, the impact on the proposed algorithm is analyzed later. In radar systems, a higher false alarm rate may undermine the stability and efficiency of the entire system while a lower false alarm rate might result in the missed detection of actual targets. In practical applications, the false alarm probability is typically set between  $10^{-6}$  and  $10^{-3}$ . As a rule of thumb, the minimum number of Monte Carlo simulations required for radar signal processing is  $10/P_{fa}$ , while a preferable number would be  $100/P_{fa}$ . However, for a compromise between accuracy and computational cost,  $P_{fa}$  and the number of Monte Carlo simulations are set to  $10^{-4}$  and  $10^5$ , respectively. For space target modeling, several typical line spectra models were considered, as presented in Table 2. Model 1 represents uniformly distributed harmonic energy, Model 2 represents uniformly distributed harmonic energy with certain harmonics missing, Model 3 represents the target Doppler spectrum spread as a sinc-shaped envelope with equidistant sparsity, and Model 4 represents the target Doppler spectrum as containing multiple fluctuating envelopes with equidistant sparsity.

**Table 1.** Parameters used in simulations.

Parameters	Values
Regularization parameter $\lambda$	55
Number of pulses	4000
Pulse repetition time $T_r$	40 ms
TOA period $T_o$	10 s
Number of line spectra $L$	8
Number of Doppler cells $N$	640
Probability of false alarm $P_{fa}$	$10^{-4}$
Number of Monte Carlo simulations	$10^5$

**Table 2.** Typical models of Doppler-spread targets.

Models	Doppler Cells							
	1	2	3	4	5	6	7	8
1	1	1	1	1	1	1	1	1
2	1	0	1	1	0	0	1	1
3	0.3	0.6	0.9	1	1	0.9	0.6	0.3
4	0.5	1	0.5	0.25	0.25	0.5	1	0.5

### 5.2. Effect of Regularization Parameter

For brevity in subsequent discussions, we refer to the case where the estimated number of line spectra (ENLS) matches the actual one as the match case (i.e.,  $L = \hat{L}$ ); otherwise, it is referred to as the mismatch case. First, we evaluated the effect of the regularization parameter  $\lambda$  in the OGS denoising algorithm on the performance of OGSos-GLRT. Simulations in the match case were conducted with  $\lambda$  ranging from 45 to 65 in increments of 5, and other parameters set as shown in Table 1 were conducted. Figure 6 shows the probability of detection (Pd) curves of OGSos-GLRT versus the SNR. It can be observed that, within a certain range, the regularization parameter  $\lambda$  does not significantly affect the detection performance of OGSos-GLRT. This can be attributed to the denoising algorithm for equidistant sparse line spectra, which effectively restores the indices of the line spectra within a relatively large range of  $\lambda$ . Therefore, without loss of generality,  $\lambda = 55$  was adopted in the following simulations.

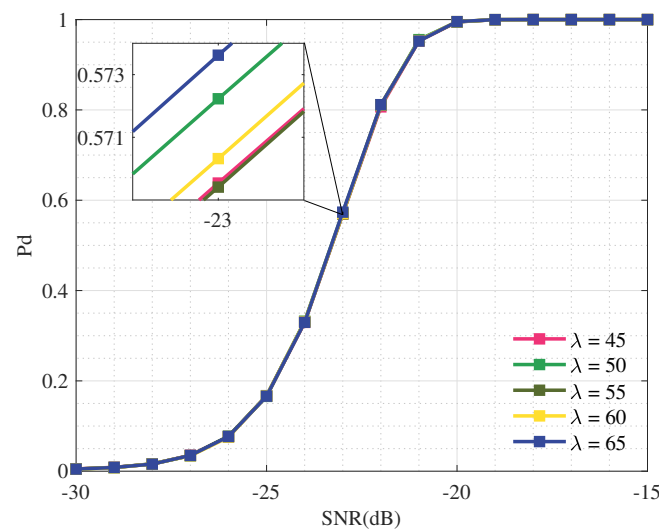


**Figure 6.** Pds versus SNR of OGSos-GLRT with Model 1 for  $\lambda = 45, 50, 55, 60, 65$ .

### 5.3. Detection Performance for Target Models

Next, the impact of different line spectra models on the detection performance of OGSos-GLRT and OS-GLRT was examined, with this factor evidently not affecting MF-GLRT or NLSD-GLRT. Models 1–4 in Table 2 were subjected to simulations in the match case, using OGSos-GLRT and OS-GLRT with the parameter settings shown in Table 1. For comparison, the simulations also involved MF-GLRT and NLSD-GLRT for Model 1. Figure 7 compares the detection performance of the four methods on different models, which reveals that, across the various models, the detection performance of OGSos-GLRT remained relatively consistent, whereas OS-GLRT showed a certain degree of performance decline, particularly with Model 1. This indicates that OGSos-GLRT exhibits greater robustness than OS-GLRT across different line spectra models.

### 5.4. Effect of Collapsing Loss

Additionally, due to the presence of collapsing loss, the detection number of Doppler cells evidently affected the performance of OGSos-GLRT, OS-GLRT, and NLSD-GLRT, while MF-GLRT remained unaffected. Figure 8 shows the detection curves of the three algorithms in the match case for the four models, with Doppler cells  $N$  doubling sequentially from 320. The results indicate that, as the number of Doppler cells increased, the collapsing loss also increased, leading to a decline in the detection performance of OGSos-GLRT, OS-GLRT, and NLSD-GLRT. Notably, OGSos-GLRT and OS-GLRT mitigated the collapsing loss to varying degrees, with OGSos-GLRT demonstrating superior performance in alleviating the collapsing loss. In addition, by comparing the subfigures in Figure 8, the robustness of OGSos-GLRT to models is again demonstrated, which is consistent with Figure 7.



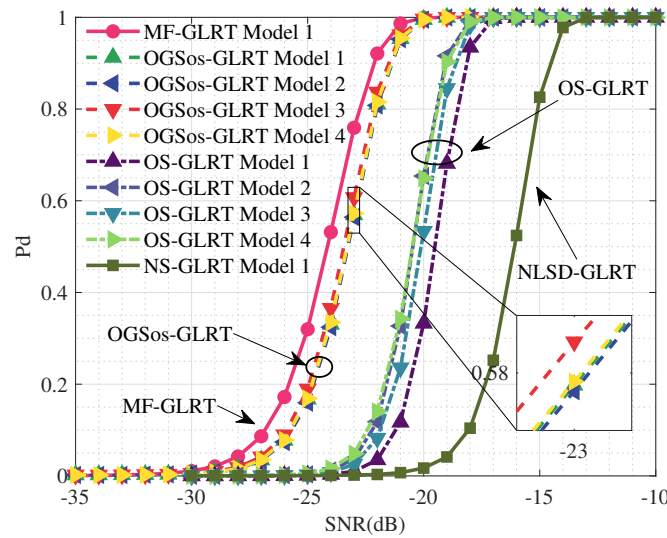


Figure 7. Pds versus SNR of MF-GLRT, OGSos-GLRT, OS-GLRT, and NLSD-GLRT for Models 1–4.

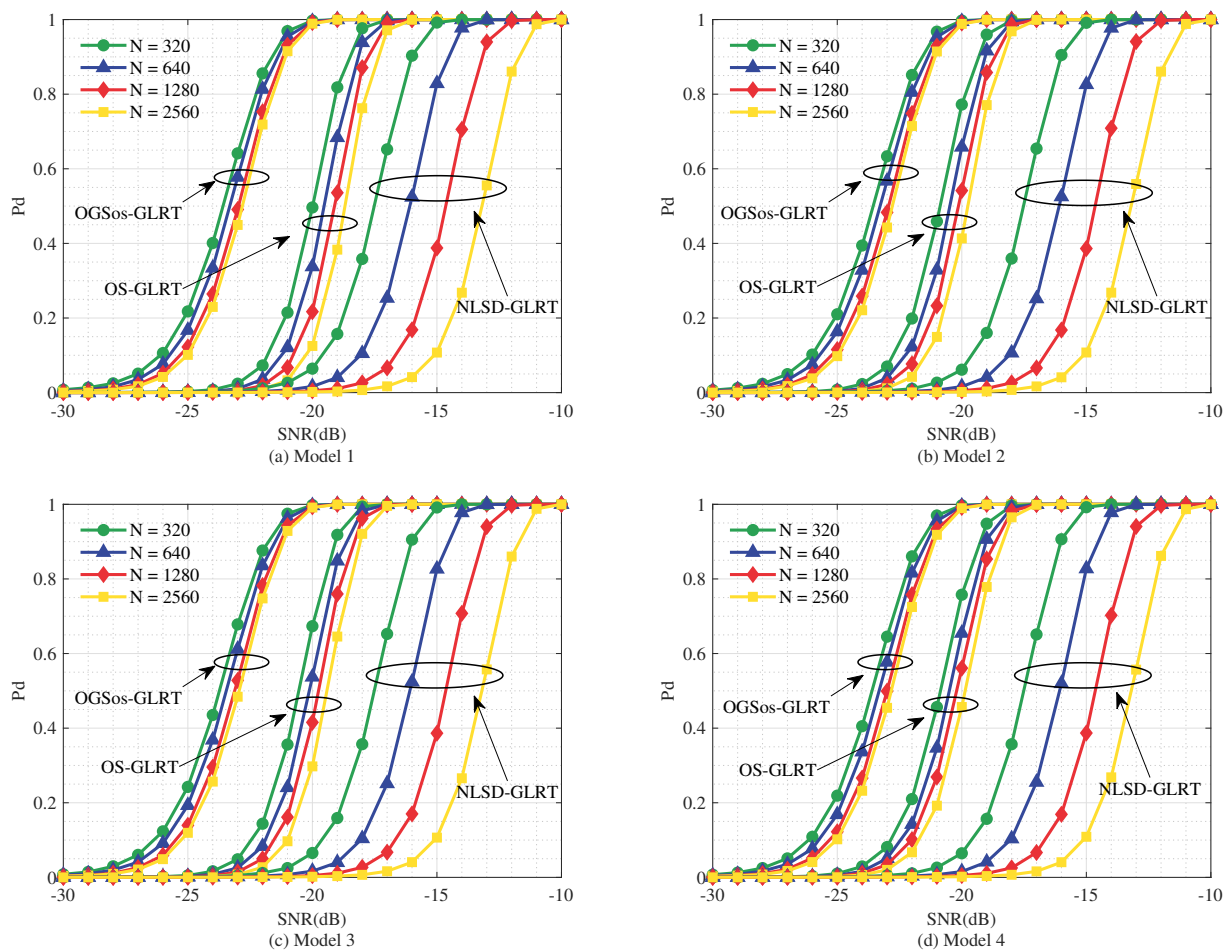
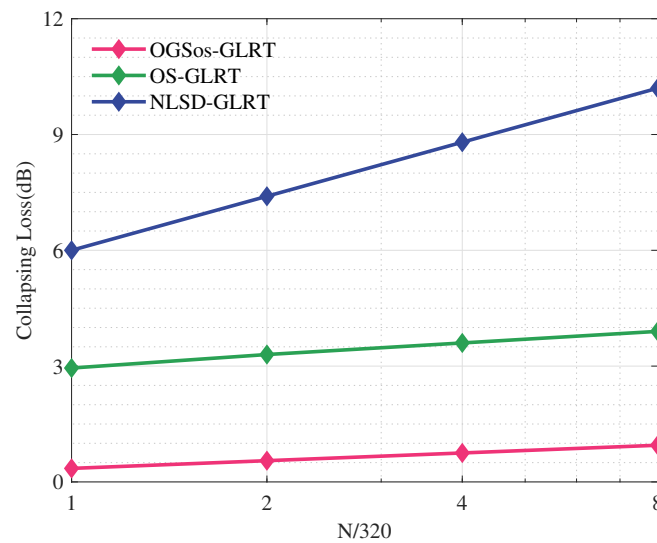


Figure 8. Pds versus SNR of OGSos-GLRT, OS-GLRT, and NLSD-GLRT with the 4 models for  $N = 320, 640, 1280, 2560$ .

To quantify the collapsing loss, we define the additional SNR required relative to MF-GLRT as the collapsing loss for OGSos-GLRT, OS-GLRT, and NLSD-GLRT in the match case, using the given false alarm probability and detection probability. Figure 9 presents the collapsing losses for OGSos-GLRT, OS-GLRT, and NLSD-GLRT with Model 3 at  $P_{fa} = 10^{-4}$  and  $P_d = 95\%$ , of which, the transverse axis represents the number of Doppler cells and

is normalized to multiples of 320. The figure shows that the collapsing losses of OGSos-GLRT, OS-GLRT, and NLS-GLRT linearly increased with the number of Doppler cells multiplying, with these increases being 0.2 dB, 0.3 dB, and 1.4 dB, respectively.



**Figure 9.** Collapsing loss versus number of Doppler cells for OGSos-GLRT, OS-GLRT, and NLS-GLRT with Model 3 at  $P_{fa} = 10^{-4}$  and  $P_d = 95\%$ .

### 5.5. Effect of TOA Period

Similarly, Figure 10 illustrates the  $P_d$ s of OGSos-GLRT for Model 3 in the match case, with the number of Doppler cells consistent with Figure 8. However, we adjusted the TOA periods to 20, 10, 5, and 2.5 seconds in this simulation. As the Doppler cells increased and the TOA period decreased, the equidistant line spectra became more sparsely distributed in the Doppler domain. Figure 10 indicates that, as the sparsity of the line spectra was enhanced, the detection performance of OGSos-GLRT did not degrade due to the collapsing loss. However, the result for OS-GLRT remained consistent with that depicted in Figure 8, still suffering from the collapsing loss. This suggests that OGSos-GLRT not only exhibits better robustness with respect to targets having different TOA periods but also demonstrates superior detection performance for Doppler line spectra with higher sparsity.

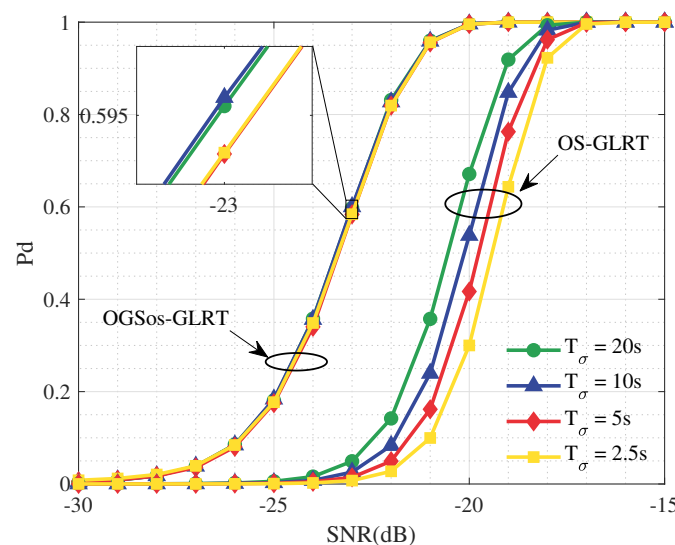


**Figure 10.**  $P_d$ s versus SNR of OGSos-GLRT and OS-GLRT with Model 3 for  $T_\sigma = 20, 10, 5, 2.5$  s.

### 5.6. Detection Performance for Numbers of Line Spectra

Furthermore, the detection performance of OGSos-GLRT, OS-GLRT, and MF-GLRT for Model 1 and with different numbers of line spectra in the match case was also investigated. Figure 11 presents the  $P_d$ s versus the SNR of the above three detectors, with the numbers of line spectra being  $L = 4, 8, 16, 32$ . The results indicate that, as the number of line spectra increased, the detection performance of MF-GLRT, OGSos-GLRT, and OS-GLRT decreased by varying degrees. This can be attributed to the following: for a given SNR, a larger number of line spectra means that each line spectrum has less energy and that more noise energy is introduced. Two extreme cases are as follows: (1)  $L = 1$ —in this case, the target Doppler spectrum does not spread and coherent integration suffers no loss, resulting in the highest detection probability; and (2)  $L = N$ —in this case, the target fully spreads its energy evenly across each Doppler cell, leading to the worst detection performance. Nonetheless, the detection performance of OGSos-GLRT surpassed that of OS-GLRT and approached that of MF-GLRT as the number of line spectra increased.

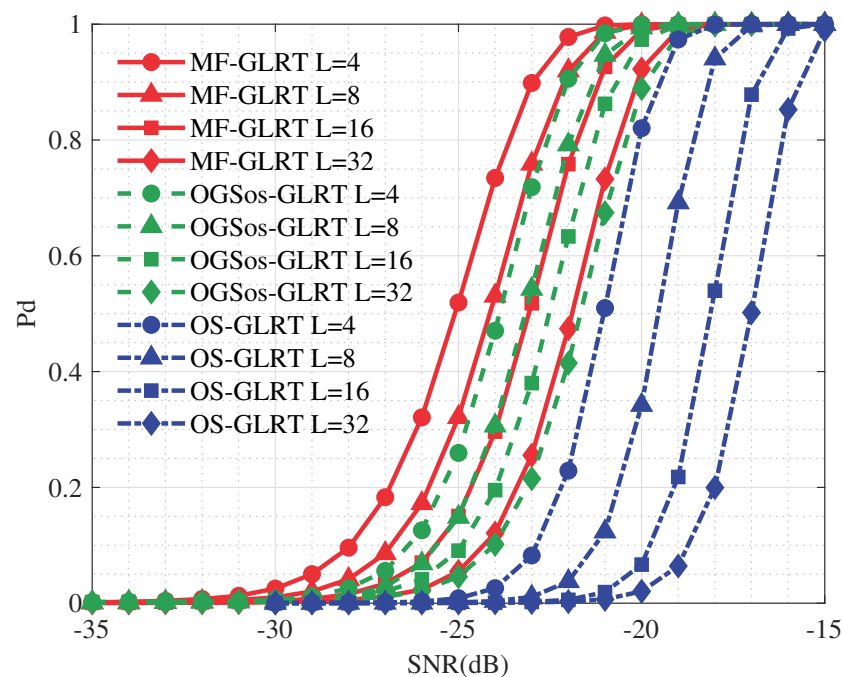


**Figure 11.**  $P_d$ s versus SNR of MF-GLRT, OGSos-GLRT, and OS-GLRT with Model 1 for  $L = 4, 8, 16, 32$ .

### 5.7. Detection Performance in Mismatch Cases

In practice, the number of line spectra of space targets is often unknown. Therefore, the ENLS is used instead of the actual number when utilizing OGSos-GLRT or OS-GLRT for target detection, which might cause mismatch loss. To investigate the detection performance of OGSos-GLRT in the mismatch case, simulations for Model 1 using the OGSos-GLRT and OS-GLRT algorithms with  $\hat{L} = 2, 4, 8, 12, 16, 32$  were carried out, and the  $P_d$ s are shown in Figure 12. It can be observed that the detection performance of both OGSos-GLRT and OS-GLRT decreased in the mismatch case, especially when the ENLS was significantly smaller than the actual value. The subplot in Figure 12 quantitatively illustrates the mismatch loss of OGSos-GLRT and OS-GLRT for a given detection probability of 0.95, indicating that the mismatch loss of OGSos-GLRT was about 2.5 dB when  $\hat{L} = 2$ . Despite the superior robustness of OS-GLRT with respect to variation in the ENLS, the overall detection performance of OGSos-GLRT remained better than that of OS-GLRT.

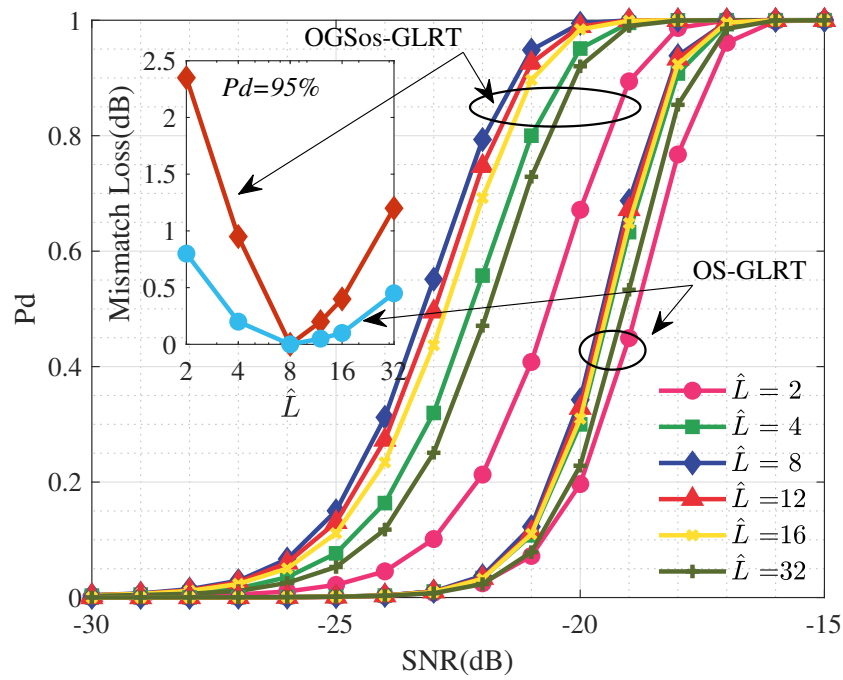


**Figure 12.**  $P_d$ s versus SNR of OGSos-GLRT and OS-GLRT with Model 1 for  $L = 8$ ,  $\hat{L} = 2, 4, 8, 12, 16, 32$ ; mismatch loss of OGSos-GLRT and OS-GLRT versus  $\hat{L}$  with  $P_d = 95\%$ .

### 5.8. Modified OGSos-GLRT

To enhance the robustness of OGSos-GLRT in the mismatch case, we iteratively cycled through the ENLS (from 1 to a predefined maximum value  $\hat{L}_m$ ) during the detection process. Each cycle involved the generation of test statistics  $\Lambda_{\hat{L}}$  and detection thresholds  $\gamma_{\hat{L}}$ , followed by decision making. If  $\Lambda_{\hat{L}} \geq \gamma_{\hat{L}}$ , then we decided  $H_1$  and terminated the loop; otherwise, the next iteration began with  $\hat{L} + 1$ . Iteration was continued until  $\hat{L} = \hat{L}_m$  and, if  $\Lambda_{\hat{L}}$  remained less than  $\gamma_{\hat{L}}$  at this point, then we decided  $H_0$ . The aforementioned detection algorithm is referred to as the modified OGSos-GLRT, the schematic of which is outlined in Figure 13. Figure 14 illustrates the  $P_d$ s of OGSos-GLRT in the match case and the modified OGSos-GLRT for Model 1 with varying numbers of line spectra. The results indicate that the detection performance of the modified OGSos-GLRT closely aligned with that of OGSos-GLRT, with some slight advantages observed at low SNRs. This is attributed to the fact that, under a low SNR, the detection performance may deteriorate when Doppler cells containing line spectra are completely masked by noise or cells containing only noise are integrated into the test statistics. However, the modified OGSos-GLRT partially mitigates such loss through leveraging the minimal ENLS for detection.

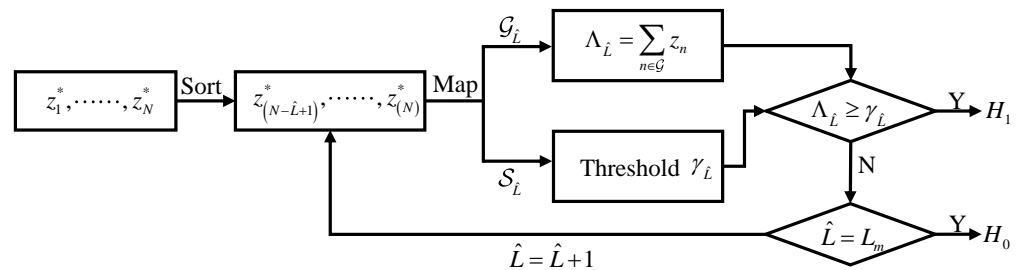


**Figure 13.** Schematic of the modification to OGSos-GLRT.

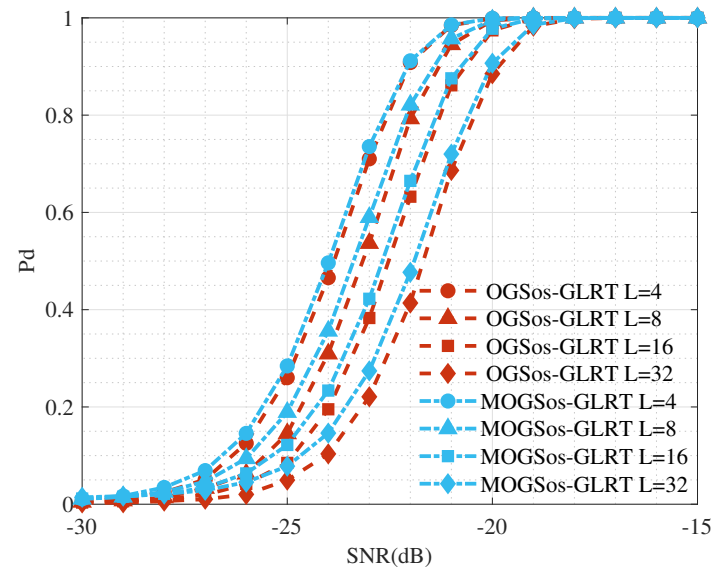


**Figure 14.** Pds versus SNR of OGSos–GLRT (in the match case) and modified OGSos–GLRT with Model 1 for  $L = 4, 8, 16, 32$ .

## 6. Conclusions

In this study, we presented a robust generalized likelihood ratio test based on overlapping group shrinkage denoising and order statistics (OGSos-GLRT). This method addresses the problem related to the detection of a Doppler spectrum spreading into equidistant sparse line spectra resulting from periodic changes in TOA during the prolonged coherent integration of space targets. To elaborate, we initially utilize the orbital information of space targets to perform the translational compensation and coherent integration of target echoes, yielding corresponding Doppler sequences. Subsequently, leveraging the equidistant sparse characteristics of the Doppler sequences, we employ the OGS algorithm for denoising. Following denoising, the sequences undergo energy sorting, identifying some of the largest values that correspond to the Doppler cell indices before denoising, which are then integrated into the GLRT for the detection of targets. Furthermore, in order to enhance the robustness of the proposed algorithm in terms of the ENLS, we sequentially evaluate the test statistics against the detection threshold using an increasing ENLS until a decision is reached.

We evaluated the performance of the proposed algorithm through Monte Carlo simulations. First, the detection performance of OGSos-GLRT was found to be superior to that of OS-GLRT and NLSD-GLRT and approached that of MF-GLRT, especially for targets with a large number of line spectra. Second, OGSos-GLRT exhibited robustness with respect to the regularization parameter in the OGS denoising algorithm—an advantage that also applies to space targets with different line spectra models and TOA periods. Furthermore, compared with the OS-GLRT and NLSD-GLRT detectors, OGSos-GLRT was the most effective in reducing the collapsing loss due to the presence of Doppler cells that only contain noise. In addition, OGSos-GLRT performed well for line spectra with more sparsity. Despite showing a higher performance loss than OS-GLRT when the ENLS mismatches the actual value, the overall detection performance of OGSos-GLRT was still superior to that of OS-GLRT, and the mismatch loss was effectively addressed by the modified OGSos-GLRT.

This study considers the case of precise compensation for target translational effects. Even if there is a first-order residual translational phase in the target echoes, the line spectra only undergo a Doppler shift in the frequency domain. Notably, the OGS denoising algorithm employs a sliding window across the entire sequence and, therefore, its denoising performance is translation-invariant; that is, it is dependent on the positions of line spectra and does not affect the detection performance. However, when higher-order phase residues are present, the equidistant sparsity of the Doppler spectrum may be disrupted, which

will lead to a decline in detection performance. Future research will focus on situations involving residual higher-order phases resulting from translational motions.

**Author Contributions:** Conceptualization, L.B. and T.F.; methodology, L.B. and T.F.; software, L.B.; validation, L.B., J.H. and S.Z.; formal analysis, L.B. and J.H.; investigation, L.B. and S.Z.; resources, L.B. and D.C.; data curation, L.B. and H.C.; writing—original draft preparation, L.B., H.C. and D.C.; writing—review and editing, T.F. and S.Z.; visualization, L.B. and J.H.; supervision, T.F. and D.C.; project administration, L.B. All authors have read and agreed to the published version of the manuscript.

**Funding:** This research received no external funding.

**Institutional Review Board Statement:** Not applicable.

**Informed Consent Statement:** Not applicable.

**Data Availability Statement:** No new data were created or analyzed in this study. Data sharing is not applicable to this article.

**Conflicts of Interest:** The authors declare no conflicts of interest.

## Abbreviations

The following abbreviations are used in this manuscript:

TOA	Target observation attitude
CPI	Coherent processing interval
SNR	Signal-to-noise ratio
GLRT	Generalized likelihood ratio test
ENLS	Estimated number of line spectra
OGS	Overlapping group shrinkage
SSA	Space situational awareness
RM	Range migration
DFM	Doppler frequency migration
TFD	Time–frequency distribution
HRRP	High-resolution range profile
CFAR	Constant false alarm rate
SDD-GLRT	Scatterer density-dependent GLRT
OS-GLRT	Order statistics GLRT
ASCE-GLRT	Adaptive scatterers estimation GLRT
ASCE-GLRT	Adaptive Doppler steering matrix estimation GLRT
OGSos-GLRT	Overlapping group shrinkage and order statistics GLRT
MF-GLRT	Match filter GLRT
NLSD-GLRT	Non-line spectra-dependent GLRT

## Appendix A

In this appendix, the following assumptions on the penalty function are made:

- $\phi$  is continuous on  $\mathbb{R}$ ;
- $\phi$  is even;
- $\phi$  has a unit slope at zero;
- $\phi$  has a second derivative with a lower bound of  $-a$  on  $\mathbb{R} \setminus \{0\}$ ;
- $\phi$  increases monotonically and is concave on the positive  $x$ -axis;
- $\phi$  equals the absolute value function when  $a = 0$ .

## Appendix B

In this appendix, the derivation of the condition under which parameter  $a$  makes the objective function a strictly convex function  $\mathcal{J}$  is given.

$$\mathcal{J}(\bar{\mathbf{X}}) = \frac{1}{2} \sum_{n=1}^N \left[ (\bar{y}_n - \bar{x}_n)^2 + (\bar{y}_{N+n} - \bar{x}_{N+n})^2 \right] + \lambda \sum_{n=1}^N \phi(\bar{\zeta}_n; a), \quad (\text{A1})$$



$$\mathcal{J}(\bar{\mathbf{X}}) = \frac{1}{2} \sum_{n=1}^N (\bar{x}_n^2 + \bar{x}_{N+n}^2) + \mathcal{R}(\bar{\mathbf{X}}) + \lambda \sum_{n=1}^N \phi(\xi_n; a), \quad (\text{A2})$$

where  $\mathcal{R}(\bar{\mathbf{X}})$  is linear with  $\bar{\mathbf{X}}$ . For a strictly convex function, the addition of a linear term preserves its strict convexity. Let the sum of the remaining two terms in  $\mathcal{J}$  be  $\mathcal{Q}$ ; that is,

$$\mathcal{Q}(\bar{\mathbf{X}}) = \frac{1}{2} \sum_{n=1}^N (\bar{x}_n^2 + \bar{x}_{N+n}^2) + \lambda \sum_{n=1}^N \phi(\xi_n; a). \quad (\text{A3})$$

According to  $\sum_{k=0}^{K-1} b_k = M$ ,  $\mathcal{Q}$  can be rewritten as

$$\begin{aligned} \mathcal{Q}(\bar{\mathbf{X}}) &= \frac{1}{2M} \sum_{n=1}^N \sum_{k=0}^{K-1} b_k (\bar{x}_n^2 + \bar{x}_{N+n}^2) + \lambda \sum_{n=1}^N \phi(\xi_n; a) \\ &= \frac{1}{2M} \sum_{n=1}^{N-K+1} \sum_{k=0}^{K-1} b_k (\bar{x}_{n+k}^2 + \bar{x}_{N+n+k}^2) + \lambda \sum_{n=1}^{N-K+1} \phi(\xi_n; a) \\ &= \sum_{n=1}^{N-K+1} \left[ \frac{1}{2M} \sum_{k=0}^{K-1} b_k (\bar{x}_{n+k}^2 + \bar{x}_{N+n+k}^2) + \lambda \phi(\xi_n; a) \right] \\ &= \sum_{n=1}^{N-K+1} \mathcal{W}(\bar{x}_n) \end{aligned} \quad (\text{A4})$$

where  $\mathcal{W}(\bar{x}_n) = \frac{1}{2M} \sum_{k=0}^{K-1} b_k (\bar{x}_{n+k}^2 + \bar{x}_{N+n+k}^2) + \lambda \phi(\xi_n; a)$ . Then,  $\mathcal{Q}$  is strictly convex if  $\mathcal{W}$  is strictly convex. We rewrite  $\mathcal{W}$  as:

$$\begin{aligned} \mathcal{W}(\bar{x}_n) &= \frac{1}{2M} \sum_{k \in \{k: b_k=1\}} b_k (\bar{x}_{n+k}^2 + \bar{x}_{N+n+k}^2) \\ &\quad + \lambda \phi \left( \left[ \sum_{k \in \{k: b_k=1\}} b_k (\bar{x}_{n+k}^2 + \bar{x}_{N+n+k}^2) \right]^{1/2}; a \right), \end{aligned} \quad (\text{A5})$$

and let  $\xi_n' = \left[ \sum_{k \in \{k: b_k=1\}} b_k (\bar{x}_{n+k}^2 + \bar{x}_{N+n+k}^2) \right]^{1/2}$  and  $\gamma = \frac{1}{M}$ . Then, Equation (A5) can be transformed as follows:

$$\mathcal{F}(\xi) = \frac{\gamma}{2} \xi^2 + \lambda \phi(\xi; a), \quad (\text{A6})$$

with its second derivative

$$\mathcal{F}''(\xi) = \gamma + \lambda \phi''(\xi; a), \xi \neq 0. \quad (\text{A7})$$

When  $\xi \neq 0$ , the sufficient condition for  $\mathcal{F}''(\xi) > 0$  is  $\phi''(\xi; a) > -\gamma/\lambda$ ; when  $\xi = 0$ ,  $\mathcal{F}'(0^-) < \mathcal{F}'(0^+)$ , as stated in Lemma A [34],  $\mathcal{F}$  is strictly convex. In conclusion, the sufficient condition for  $\mathcal{F}$  to be strictly convex is  $0 < a \leq \frac{1}{\lambda M}$ . When  $a = 0$ ,  $\phi(x; 0) = |x|$  is regarded as an extreme case. Ultimately, when  $0 \leq a \leq \frac{1}{\lambda M}$ ,  $\mathcal{F}$  is a strictly convex function; that is,  $\mathcal{J}$  is strictly convex.

## References

1. Lin, B.; Wang, J.; Wang, H.; Zhong, L.; Yang, X.; Zhang, X. Small Space Target Detection Based on a Convolutional Neural Network and Guidance Information. *Aerospace* **2023**, *10*, 426. [CrossRef]
2. Perry, R.; DiPietro, R.; Fante, R. SAR imaging of moving targets. *IEEE Trans. Aerosp. Electron. Syst.* **1999**, *35*, 188–200. [CrossRef]
3. Kirkland, D. Imaging moving targets using the second-order keystone transform. *IET Radar Sonar Navig.* **2011**, *5*, 902–910. [CrossRef]

4. Xu, J.; Yu, J.; Peng, Y.N.; Xia, X.G. Radon-Fourier Transform for Radar Target Detection, I: Generalized Doppler Filter Bank. *IEEE Trans. Aerosp. Electron. Syst.* **2011**, *47*, 1186–1202. [\[CrossRef\]](#)
5. Kong, L.; Li, X.; Cui, G.; Yi, W.; Yang, Y. Coherent Integration Algorithm for a Maneuvering Target With High-Order Range Migration. *IEEE Trans. Signal Process.* **2015**, *63*, 4474–4486. [\[CrossRef\]](#)
6. Li, X.; Cui, G.; Kong, L.; Yi, W. Fast Non-Searching Method for Maneuvering Target Detection and Motion Parameters Estimation. *IEEE Trans. Signal Process.* **2016**, *64*, 2232–2244. [\[CrossRef\]](#)
7. Huang, P.; Liao, G.; Yang, Z.; Xia, X.G.; Ma, J.T.; Ma, J. Long-Time Coherent Integration for Weak Maneuvering Target Detection and High-Order Motion Parameter Estimation Based on Keystone Transform. *IEEE Trans. Signal Process.* **2016**, *64*, 4013–4026. [\[CrossRef\]](#)
8. Li, X.; Cui, G.; Yi, W.; Kong, L. Sequence-Reversing Transform-Based Coherent Integration for High-Speed Target Detection. *IEEE Trans. Aerosp. Electron. Syst.* **2017**, *53*, 1573–1580. [\[CrossRef\]](#)
9. Huang, P.; Xia, X.G.; Liao, G.; Yang, Z.; Zhang, Y. Long-Time Coherent Integration Algorithm for Radar Maneuvering Weak Target With Acceleration Rate. *IEEE Trans. Geosci. Remote Sens.* **2019**, *57*, 3528–3542. [\[CrossRef\]](#)
10. Zhang, J.; Ding, T.; Zhang, L. Longtime Coherent Integration Algorithm for High-Speed Maneuvering Target Detection Using Space-Based Bistatic Radar. *IEEE Trans. Geosci. Remote Sens.* **2022**, *60*, 5100216. [\[CrossRef\]](#)
11. Uno, K.; Matsuoka, T.; Uchida, A.; Yoshida, K. Structure from Motion-based Motion Estimation and 3D Reconstruction of Unknown Shaped Space Debris. *arXiv* **2024**, arXiv:2408.01035.
12. Serrano, A.; Kobsa, A.; Uysal, F.; Cerutti-Maori, D.; Ghio, S.; Kintz, A.; Morrison Jr., R.L.; Welch, S.; van Dorp, P.; Hogan, G.; et al. Long baseline bistatic radar imaging of tumbling space objects for enhancing space domain awareness. *IET Radar Sonar Navig.* **2024**, *18*, 598–619. [\[CrossRef\]](#)
13. Zhou, X.; Wang, Y.; Yeh, C.; Lu, X. Precession Parameter Estimation From Wideband Measurements for 3-D ISAR Imaging of Cone-Shaped Targets. *IEEE Geosci. Remote Sens. Lett.* **2022**, *19*, 4501305. [\[CrossRef\]](#)
14. Lin, L.; Sun, G.; Cheng, Z.; He, Z. Long-Time Coherent Integration for Maneuvering Target Detection Based on ITRT-MRFT. *IEEE Sens. J.* **2020**, *20*, 3718–3731. [\[CrossRef\]](#)
15. Van Der Spek, G.A. Detection of a Distributed Target. *IEEE Trans. Aerosp. Electron. Syst.* **1971**, AES-7, 922–931. [\[CrossRef\]](#)
16. Hughes, P. A High-Resolution Radar Detection Strategy. *IEEE Trans. Aerosp. Electron. Syst.* **1983**, AES-19, 663–667. [\[CrossRef\]](#)
17. Dai, F.; Liu, H.; Wu, S. Order-Statistic-Based Detector for Range Spread Target. *J. Electron. Inf. Technol.* **2009**, *31*, 2488–2492.
18. Shui, P.L.; Liu, H.W.; Bao, Z. Range-Spread Target Detection Based on Cross Time-Frequency Distribution Features of Two Adjacent Received Signals. *IEEE Trans. Signal Process.* **2009**, *57*, 3733–3745. [\[CrossRef\]](#)
19. Zuo, L.; Li, M.; Zhang, X.; Zhang, P.; Wu, Y. CFAR Detection of Range-Spread Targets Based on the Time-Frequency Decomposition Feature of Two Adjacent Returned Signals. *IEEE Trans. Signal Process.* **2013**, *61*, 6307–6319. [\[CrossRef\]](#)
20. Shui, P.L.; Xu, S.W.; Liu, H.W. Range-Spread Target Detection using Consecutive HRRPs. *IEEE Trans. Aerosp. Electron. Syst.* **2011**, *47*, 647–665. [\[CrossRef\]](#)
21. Yang, X.; Wen, G.; Ma, C.; Hui, B.; Ding, B.; Zhang, Y. CFAR Detection of Moving Range-Spread Target in White Gaussian Noise Using Waveform Contrast. *IEEE Geosci. Remote Sens. Lett.* **2016**, *13*, 282–286. [\[CrossRef\]](#)
22. De Maio, A. Polarimetric adaptive detection of range-distributed targets. *IEEE Trans. Signal Process.* **2002**, *50*, 2152–2159. [\[CrossRef\]](#)
23. Tang, M.; Rong, Y.; Zhou, J.; Li, X.R. Invariant Adaptive Detection of Range-Spread Targets Under Structured Noise Covariance. *IEEE Trans. Signal Process.* **2017**, *65*, 3048–3061. [\[CrossRef\]](#)
24. Sun, S.; Liu, J.; Liu, W.; Jian, T. Robust detection of distributed targets based on Rao test and Wald test. *Signal Process.* **2021**, *180*, 107801. [\[CrossRef\]](#)
25. Chen, X.; Gai, J.; Liang, Z.; Liu, Q.; Long, T. Adaptive Double Threshold Detection Method for Range-Spread Targets. *IEEE Signal Process. Lett.* **2022**, *29*, 254–258. [\[CrossRef\]](#)
26. Gu, X.; Tao, J.; You, H. Double Threshold CFAR Detector of Range-spread Target and Its Performance Analysis. *J. Electron. Inf. Technol.* **2012**, *34*, 1318–1323. [\[CrossRef\]](#)
27. Shuai, X.; Kong, L.; Yang, J. Adaptive detection for distributed targets in Gaussian noise with Rao and Wald tests. *Sci. China Inf. Sci.* **2012**, *55*, 1290–1300. [\[CrossRef\]](#)
28. Liu, J.; Liu, W.; Tang, B.; Zheng, J.; Xu, S. Distributed Target Detection Exploiting Persymmetry in Gaussian Clutter. *IEEE Trans. Signal Process.* **2019**, *67*, 1022–1033. [\[CrossRef\]](#)
29. Gerlach, K. Spatially distributed target detection in non-Gaussian clutter. *IEEE Trans. Aerosp. Electron. Syst.* **1999**, *35*, 926–934. [\[CrossRef\]](#)
30. He, Y.; Jian, T.; Su, F.; Qu, C.; Gu, X. Novel Range-Spread Target Detectors in Non-Gaussian Clutter. *IEEE Trans. Aerosp. Electron. Syst.* **2010**, *46*, 1312–1328. [\[CrossRef\]](#)
31. Ren, Z.; Yi, W.; Zhao, W.; Kong, L. Range-Spread Target Detection Based on Adaptive Scattering Centers Estimation. *IEEE Trans. Geosci. Remote Sens.* **2023**, *61*, 5100414. [\[CrossRef\]](#)
32. Ren, Z.; Yi, W.; Kong, L.; Farina, A.; Orlando, D. Adaptive Range and Doppler Distributed Target Detection in Non-Gaussian Clutter. *IEEE Trans. Signal Process.* **2023**, *71*, 2376–2390. [\[CrossRef\]](#)
33. Chen, P.Y.; Selesnick, I.W. Group-Sparse Signal Denoising: Non-Convex Regularization, Convex Optimization. *IEEE Trans. Signal Process.* **2014**, *62*, 3464–3478. [\[CrossRef\]](#)

34. Chen, P.Y.; Selesnick, I.W. Translation-invariant shrinkage/thresholding of group sparse signals. *Signal Process.* **2014**, *94*, 476–489. [[CrossRef](#)]
35. He, W.; Ding, Y.; Zi, Y.; Selesnick, I.W. Sparsity-based algorithm for detecting faults in rotating machines. *Mech. Syst. Signal Process.* **2016**, *72–73*, 46–64. [[CrossRef](#)]
36. Li, Z.; Li, J.; Ding, W.; Cheng, X.; Meng, Z. A sparsity-enhanced periodic OGS model for weak feature extraction of rolling bearing faults. *Mech. Syst. Signal Process.* **2022**, *169*, 108733. [[CrossRef](#)]
37. Wang, Q.; Xing, M.; Lu, G.; Bao, Z. Single Range Matching Filtering for Space Debris Radar Imaging. *IEEE Geosci. Remote Sens. Lett.* **2007**, *4*, 576–580. [[CrossRef](#)]
38. Bell, M.; Grubbs, R. JEM modeling and measurement for radar target identification. *IEEE Trans. Aerosp. Electron. Syst.* **1993**, *29*, 73–87. [[CrossRef](#)]
39. Zhao, Z.; Wu, S.; Qiao, B.; Wang, S.; Chen, X. Enhanced Sparse Period-Group Lasso for Bearing Fault Diagnosis. *IEEE Trans. Ind. Electron.* **2019**, *66*, 2143–2153. [[CrossRef](#)]
40. David, H.A.; Nagaraja, H.N. *Order Statistics*, 3rd ed.; John Wiley & Sons, Inc.: Hoboken, NJ, USA, 2003.

**Disclaimer/Publisher’s Note:** The statements, opinions and data contained in all publications are solely those of the individual author(s) and contributor(s) and not of MDPI and/or the editor(s). MDPI and/or the editor(s) disclaim responsibility for any injury to people or property resulting from any ideas, methods, instructions or products referred to in the content.